New Journal of Physics
The open-access journal for physics

Quantitative ellipsometric microscopy at the glass–water interface

F Linke[1] **and R Merkel**[2]

Institut für Schichten und Grenzflächen, Institut 4: Biologische Schichten (ISG4), Forschungszentrum Jülich GmbH, D-52425 Jülich, Germany
E-mail: r.merkel@fz-juelich.de

New Journal of Physics **7** (2005) 128
Received 23 February 2005
Published 20 May 2005
Online at http://www.njp.org/
doi:10.1088/1367-2630/7/1/128

Abstract. Ellipsometric microscopy is a technique for simultaneous measurement of thin film thickness and index of refraction at a lateral resolution of approximately 1 μm. Up to now this technique has been used on silicon–air interfaces. However, biological processes take place often in aqueous solution and are studied at the glass–water interface. Due to the very low reflectivity of this interface we had to improve ellipsometric microscopy substantially. Here we present our approach to suppress the intensity of internal stray light by several orders of magnitude and show quantitative and laterally resolved ellipsometric measurements at the glass–water interface. When instrumental polarization was taken into account, an accuracy of $\delta\Psi = 0.41^\circ$ and $\delta\Delta = 4.3^\circ$ was achieved.

[1] Present address: Laboratoire Kastler Brossel de l'E.N.S., 24, rue Lhomond, 75231 Paris, France.
[2] Author to whom any correspondence should be addressed.

1367-2630/05/010128+17$30.00

Contents

1. Introduction **2**
2. Basic ellipsometry **3**
3. Experimental setup **5**
4. Sample preparation **7**
5. Results **8**
5.1. Improvement of stray light to signal ratio 8
5.2. Ellipsometric performance 10
5.3. Accuracy 12
6. The influence of the stray light pinhole on the lateral resolution **15**
7. Conclusion **16**
Acknowledgments **16**
References **17**

1. Introduction

Thin film properties are crucial in many biological problems, especially those related to the behaviour of living cells. For example, coatings from proteins or polymers are the standard method for biofunctionalization and biocompatibilization of surfaces. Other areas of interest concern the interaction of microstructured thin films with either living cells [1]–[3] or cell model systems [4]–[6]. Moreover, living cells are known to produce thin films during locomotion which are also known as 'migration tracks' and exhibit pronounced inhomogeneities on the μm length scale [7, 8]. In this context it is of special interest to investigate such films at the glass–water interface, thus allowing for measurements of biologically relevant systems in this well-characterized environment. An established tool for such investigations is the reflection interference contrast microscope [9]–[11]. Relative height and thickness changes can be measured at high lateral resolution (0.5 μm) with nanometre vertical resolution. In recent times the main drawback of the technique—ambiguous height determination from the measured intensity—was eliminated by extension to dual wavelength operation [12].

Here we present the adaption of another combination of microscopy with a sensitive optical technique for thin film studies in order to allow for investigations at the glass–water interface: ellipsometric microscopy. The ability of ellipsometry to measure simultaneously thickness and refractive index of thin layers adds another dimension to the obtained results. It allows discrimination of different materials or enables indirect measurement of quantities affecting the refracting index, e.g. temperature or concentration.

Many approaches to empower ellipsometry with spatial resolution have been reported in the past [13]–[20] and their characteristics were compared to our instrument in [21], where we demonstrated decent ellipsometric performance at the silicon–air interface. This required correction for several systematic errors. The most important issues were a slight nonlinearity of the utilized CCD camera and the instrumental polarization of the imaging optics. At the glass–water interface quantitative ellipsometry has not been possible up to now for the following reason. The small difference in refractive index between substrate (glass) and ambient medium (water) results in very weakly reflecting samples. Thus, the intensity of the true image became comparable

to the internal reflections created at the optical components of the setup, even though we had used optimized lenses. Here we present a solution to this problem and show that quantitative and spatially resolved ellipsometry is also possible at the glass–water interface. This is an important step towards the application of ellipsometric microscopy to biological samples and processes.

2. Basic ellipsometry

In reflection ellipsometry, a sample is illuminated with monochromic parallel light of a well-defined polarization. Ellipsometric setups measure the state of polarization after reflection at the sample. Using the Fresnel equations for the propagation of light in layered media [22], optical properties (refractive index n, thickness d) of layers thinner than the wavelength of the light itself can be inferred from ellipsometric measurements. The change in polarization can be parametrized by means of the ellipsometric angles Ψ and Δ which are defined by the ratio of the reflection coefficients for light polarized perpendicular (R_s) and parallel (R_p) to the plane of incidence:

$$\tan\,\Psi e^{i\Delta} = \frac{R_p}{R_s} = \frac{|R_p|}{|R_s|} e^{i(\varphi_p - \varphi_s)}. \tag{1}$$

The change of the amplitude ratio of the electromagnetic field components is parametrized by $\tan\,\Psi$. Δ denotes the phase shift introduced between the two perpendicular components. The range of the amplitude ratio comprises the interval $[0, \infty]$, i.e. $\Psi \in [0^\circ, 90^\circ]$, while for Δ holds $\Delta \in [0^\circ, 360^\circ[$.

The design of the ellipsometric microscope is based on a rotating-analyser type ellipsometer [23]. In this kind of ellipsometer the incoming light is linearly polarized at an angle P with respect to the plane of incidence. Light reflected at the sample is analysed by a rotating polarizer, the analyser. The primary measured quantity in this instrument design is the intensity of light that passes the analyser set at an azimuthal angle A, $I(A)$. This intensity can be computed from the electrical field strength (represented as the Jones vector [22]) at the detector $\mathbf{E}_{\mathrm{Det}}$.

$$\mathbf{E}_{\mathrm{Det}} = \mathbf{R}_{-A}\,\mathbf{T}_{\mathbf{A}}\,\mathbf{R}_{A}\,\mathbf{T}_{\mathbf{S}}\,\mathbf{R}_{-P}\begin{pmatrix} E_0 \\ 0 \end{pmatrix} \tag{2}$$

with

$$\mathbf{T}_{\mathbf{A}} = \begin{pmatrix} 1 & 0 \\ 0 & 0 \end{pmatrix}, \qquad \mathbf{T}_{\mathbf{S}} = \begin{pmatrix} R_p & 0 \\ 0 & R_s \end{pmatrix} \tag{3}$$

representing Jones matrices [22] for the analyser ($\mathbf{T}_{\mathbf{A}}$) and the specimen ($\mathbf{T}_{\mathbf{S}}$). $\mathbf{R}_X$ represents the rotation matrix (with rotation angle X)

$$\mathbf{R}_X = \begin{pmatrix} \cos X & \sin X \\ -\sin X & \cos X \end{pmatrix},$$

A and P denote the azimuthal angles of the polarizer and the analyser with respect to the plane of incidence of the sample. E_0 represents the electric field strength transmitted by the polarizer. Exploiting (2) one finds for the measured intensity, $I(A)$, at the detector

$$I(A) = \varepsilon_0 cn/2 \cdot \mathbf{E}^{\dagger}_{\mathrm{Det}} \cdot \mathbf{E}_{\mathrm{Det}} = I_0(1 + a\cos(2A) + b\sin(2A)), \tag{4}$$

where

$$I_0 = \tfrac{1}{4}\varepsilon_0 cn E_0^2 (R_p R_p^* \cos^2 P + R_s R_s^* \sin^2 P), \tag{5}$$

$$a = \frac{R_p R_p^* \cos^2 P - R_s R_s^* \sin^2 P}{R_p R_p^* \cos^2 P + R_s R_s^* \sin^2 P}, \tag{6}$$

$$b = \frac{2\Re(R_p R_s^*) \cos P \sin P}{R_p R_p^* \cos^2 P + R_s R_s^* \sin^2 P}. \tag{7}$$

The electric permeability is denoted by ε_0, the speed of light by c, and n represents the refractive index of the medium in which the light propagates. The symbol $\Re(z)$ denotes the real part of the complex number z. The definition of the ellipsometric angles (1) together with (6) and (7) yields

$$\tan\ \Psi = |\tan\ P| \sqrt{\frac{1+a}{1-a}}, \tag{8}$$

$$\cos\ \Delta = \mathrm{sgn}(\cos P \sin P) \frac{b}{\sqrt{1-a^2}}. \tag{9}$$

The function $\mathrm{sgn}(x)$ returns the sign of x. Because the polarizer orientation P is known it is possible to determine Ψ and Δ of the sample by analysing the Fourier modes a, b of the normalized intensity $I(A)/I_0$ incident at the detector. The remaining quadrant ambiguity is solved by a second measurement with an inserted $\lambda/4$-wave plate (the compensator). The electrical field strength at the detector with inserted compensator is then

$$\mathbf{E}^c_{\mathrm{Det}} = \mathbf{R}_{-A}\ \mathbf{T_A}\ \mathbf{R}_A\ \mathbf{T_S}\ \mathbf{R}_{-C}\ \mathbf{T}_{\lambda/4}\ \mathbf{R}_{C-P} \begin{pmatrix} E_0 \\ 0 \end{pmatrix}, \tag{10}$$

where C is the angle the slow axis, the $\lambda/4$-wave plate, encloses with the plane of incidence and $\mathbf{T}_{\lambda/4}$ is the Jones matrix of a $\lambda/4$-wave plate

$$\mathbf{T}_{\lambda/4} = \begin{pmatrix} 1 & 0 \\ 0 & \mathrm{i} \end{pmatrix}. \tag{11}$$

The intensity at the detector is

$$I^c(A) = \varepsilon_0 cn/2 \cdot \mathbf{E}^{c\dagger}_{\mathrm{Det}} \cdot \mathbf{E}^c_{\mathrm{Det}} = I^c_0 (1 + a^c \cos(2A) + b^c \sin(2A)), \tag{12}$$

where

$$I^c_0 = \tfrac{1}{4}\varepsilon_0 cn/2 E_0^2 [\alpha R_p^* R_p + \beta R_s^* R_s], \tag{13}$$

$$a^c = \frac{\alpha R_p^* R_p - \beta R_s^* R_s}{\alpha R_p^* R_p + \beta R_s^* R_s}, \tag{14}$$

$$b^c = \frac{2\Re(R_p^* R_s \gamma)}{\alpha R_p^* R_p + \beta R_s^* R_s}. \tag{15}$$

In the previous equations, the abbreviations

$$\alpha = \cos^2(C - P)\cos^2 C + \sin^2(C - P)\sin^2 C, \tag{16}$$

$$\beta = \cos^2(C - P)\sin^2 C + \sin^2(C - P)\cos^2 C, \tag{17}$$

$$\begin{aligned}\gamma = &\sin C \cos C(\cos^2(C - P) - \sin^2(C - P)) - \mathrm{i}\sin(C - P)\cos(C - P)\\ = &\gamma_1 + \mathrm{i}\,\gamma_2\end{aligned} \tag{18}$$

have been used. Again, the definition of the ellipsometric angles (1) together with (14) and (15) are employed in order to relate Ψ and Δ with the Fourier coefficients a^C, b^C of the measured intensity $I^C(A)$:

$$\tan\Psi = \sqrt{\frac{\beta}{\alpha}}\sqrt{\frac{1 + a^c}{1 - a^c}}, \tag{19}$$

$$\sin\left(\Delta + \tan^{-1}\frac{\gamma_1}{\gamma_2}\right) = \mathrm{sgn}(\gamma_2)\frac{b^c}{\sqrt{1 - a^{c2}}}. \tag{20}$$

If the slow axis of the compensator is orientated at $C = 90^\circ$, these formulae simplify to

$$\tan\Psi^c = |\tan P|\sqrt{\frac{1 + a^c}{1 - a^c}}, \tag{21}$$

$$\sin\Delta^c = -\mathrm{sgn}(\cos P \sin P)\frac{b^c}{\sqrt{1 - a^{c2}}}. \tag{22}$$

By fitting a model function to measured $\Psi^{(c)}$ and $\Delta^{(c)}$ values one can extract up to two optical quantities of the layers constituting the sample. This model function is usually calculated by applying the Fresnel formulas, valid for stratified, planar layers [22].

3. Experimental setup

The basic idea of our setup (cf figure 1) was described before [21, 24, 25]: an inverted microscope employing epi-illumination was constructed on an optical bench. Parallel illumination of the object was achieved by focusing a parallel, polarized beam into the back focal plane of an infinity-corrected high-power microscope objective (Plan-Apochromat 63×, oil immersion, NA = 1.4, Zeiss). The crucial point in the design is that the angle of incidence can be controlled in order to maximize the ellipsometric contrast. By laterally displacing the rigid mechanically coupled system of DM and lens 2 (all lenses were achromatic doublets, $f_2 = 60$ mm) the pinhole is imaged (lenses 3 and 4, $f_3 = 50$ mm and $f_4 = 80$ mm) into the back focal plane of the objective with a certain displacement to the optical axis. This displacement causes oblique illumination of the object plane. The relation between displacement and incident angle can be obtained from Abbe's sine condition. The agreement between measured and calculated incident angle was presented in [21, 25].

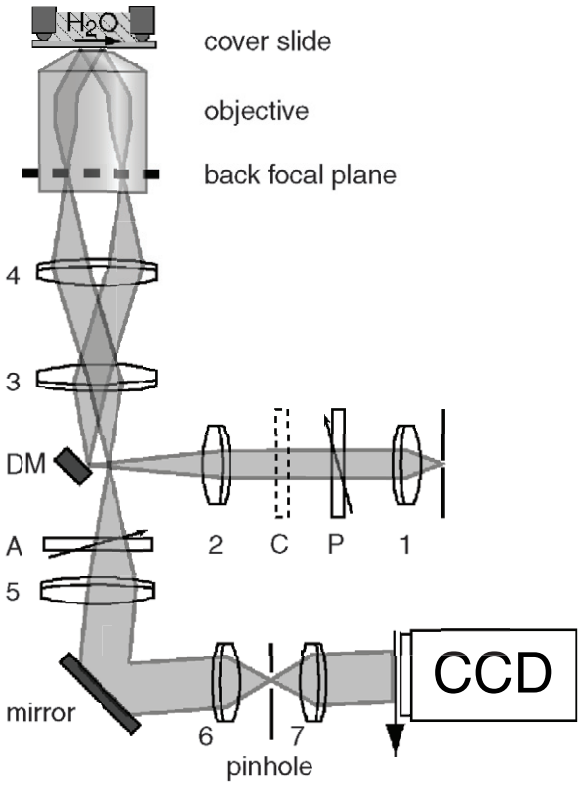

Figure 1. Design of the ellipsometric microscope: lenses 2–4 focus a parallel beam of light in an off-axis point of the back focal plane, resulting in oblique illumination of the object in the front focal plane. The object, symbolized by an arrow, is located at the upper side of the cover slide. The incoming light passes a polarizer (P) and an optional compensator (C). The angle of incidence in the front focal plane can be controlled by horizontally shifting the rigidly coupled system of lens 2 and deflection mirror (DM). Light reflected and diffracted at the object is collected by the objective, passes a computer controlled analyser (A) and is focused onto a CCD camera (lenses 5–7). Lenses 3 and 4 form a telescopic system, i.e. they influence the magnification of the microscope. The pinhole and lenses 6–7 form a stray light trap. Here the illumination beam path is depicted, i.e. wherever a focus is indicated, the illumination pinhole is imaged. Lens 7 images both pinholes to infinity and forms an image of the object on the CCD at the same time.

At the object, light was reflected and diffracted. This light was collected by the objective and imaged onto a CCD camera (C4880-50, Hamamatsu, Herrsching, Germany). Thereby the infinite space between objective and tube lens 5 ($f_5 = 150$ mm) accommodated the optical components necessary for illumination of the object and for the polarization analysis of the reflected light.

As the image is maximally blurred in this region those components created almost no image distortion. Lenses 6 and 7 ($f_{6,7} = 50\,\mathrm{mm}$) and the pinhole ($200\,\mu\mathrm{m}$) form a stray light trap. These elements were not present in our previous setup and were necessary for measurements at the glass–water interface (cf section 5.1). For each pixel the intensity $I(A)$ was measured as a function of the analyser angle A. Thus, each pixel of the CCD acted as a stand-alone ellipsometer in a rotating-analyser configuration. The polarizers were mounted in stepper motor driven goniometers (DRT 65, Owis, Staufen, Germany). A compensator (zeroth order $\lambda/4$-plate, Owis) mounted in a motorized filter wheel (Filterwheel 40, Owis) could be rotated into the optical path. All these devices were computer controlled. The calibration of the azimuthal angles P, A and C with respect to the plane of incidence was performed with the help of the calibration methods of Aspnes [26] and de Nijs *et al* [27] and was already presented by us in [21].

Ellipsometric measurements were performed by acquiring two stacks of pictures (with and without compensator), each taken typically at 18 equally spaced analyser angles between 0° and 170°. For processing of raw data, a separate image processing software was developed that computes the ellipsometric angles Ψ and Δ for each pixel of the camera. The inherent quadrant ambiguity of Δ was automatically resolved by combining the two data sets with and without the compensator. Within the software it was possible to define a model for the optical properties of the planar stratified layers of the sample and to fit the corresponding model function to either whole pictures or selected profiles of Ψ and Δ. By this procedure laterally resolved information about the refractive index n and the thickness d of any layer could be retrieved.

4. Sample preparation

The samples were thin structured films of MgF_2 ($n = 1.389$) (99.99%, Goodfellow, Bad Nauheim, Germany) deposited upon standard microscope glass cover slides (Karl Hecht KG, Sondheim, Germany). Because its refractive index is similar to hydrated proteins or lipids ($n \approx 1.40$–1.48 [28]) MgF_2 serves as a straightforward and well-controlled model system. The cover slides were cleaned by sonification (15 min) in a 2 vol% aqueous solution of cuvette cleaner (Hellmanex, Hellma GmbH, Müllheim, Germany). For removal of this detergent, the cover slides were repeatedly rinsed (10 times) and sonicated in ultra pure water (produced by a Milli-Q Reagent Grade Water System, $R > 18\,\mathrm{M\Omega\,cm^{-1}}$, pH 5.5, Millipore, Molsheim, France). This cycle was repeated three times. Thin films were structured by using an electron microscopy grid (bars: $10\,\mu\mathrm{m}$, openings: $50\,\mu\mathrm{m} \times 50\,\mu\mathrm{m}$) as mask during the deposition (thermal evaporation, BOC Edwards Auto 306 Turbo, Kirchheim, Germany: substrate temperature 25 °C, pressure 2×10^{-6} mbar, deposition rate: 4–7 nm $\mathrm{s^{-1}}$). In order to be able to determine the deposited layer thickness accurately a second mask allowed for deposition within a 6 mm × 8 mm region in close vicinity to the structured region. Ordinary ellipsometry was not applicable for determination of the film thickness on glass substrates, because the backside air–glass interface introduced a spurious reflex. The refractive indices were determined from ellipsometric measurements ($\lambda = 632.8\,\mathrm{nm}$, Plasmos GmbH, München, Germany) at auxiliary silicon substrates coated during the same deposition and closely located to the glass cover slides. Film thickness on the actual cover slides were determined by measuring the height of the macroscopic plateau next to the structure with a stylus profiler (DekTak 3030ST, 2.5 μm needle, Veeco Instruments GmbH, München, Germany). The obtained values were verified with geometry-corrected thicknesses measured with the point ellipsometer on the auxiliary silicon wafers. For the glass samples we assume the measured film

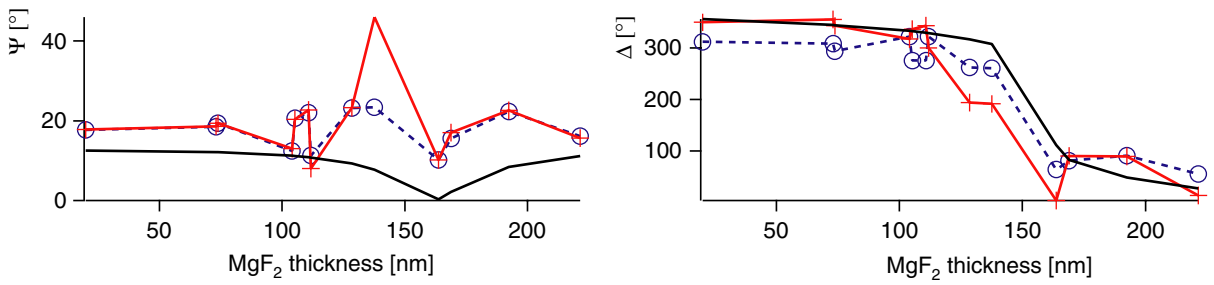

Figure 2. Measurements at the glass–water interface without the stray light trap: data obtained from samples with different heights of MgF_2 and measured with (crosses, red) and without compensator (circles, blue) in comparison to expected values (continuous line, black). The incident angle and polarizer setting angle were $\Theta = 46.6^\circ$ and $P = 45^\circ$. All shown data points were already zone averaged, corrected for nonlinearities and by background subtraction for internal reflections. Nevertheless, the data were very noisy and could not be corrected for the instrumental polarization. This demonstrates the necessity to eliminate stray light.

thicknesses to be accurate up to ± 5 nm, which is the accuracy estimated from repeated stylus profiler measurements.

For the actual measurements, the coated cover slides were mounted in a chamber which can be filled with fluids. Stress, which could make the cover slide birefringent, is only exerted at its very edge and therefore it is assumed to be free of birefringence.

5. Results

5.1. Improvement of stray light to signal ratio

Our previous experiments [25] showed that the elimination of stray light is crucial in order to allow for accurate measurements at the glass–water interface. Although we used only lenses with anti-reflection coatings optimized for the employed wavelength ($\lambda = 546.1$ nm) a prohibitive level of stray light was present in our original setup. The measured Ψ and Δ values were extremely noisy and exhibited considerable deviations from expected values (cf figure 2). Therefore, it was necessary to find a way to block this stray light. This was achieved by spatially filtering the reflected light very close to the detector. The filtering aperture had to be integrated into the setup in such a way that not too much spatial or ellipsometric information was lost. The appropriate location for such an aperture was within a plane conjugated to the back focal plane of the objective. In such a plane the partition of the light carrying the ellipsometric information, i.e. the light reflected at the object, is focused on a tiny spot. Unfortunately, the setup presented earlier in [25] did not accommodate any accessible location. Hence, we created a new plane conjugated to the back focal plane by inserting a telescopic system just before the CCD camera (cf figure 1). At the focus we placed a pinhole with 200 μm diameter. Because the sample is illuminated under a certain angle of incidence $\Theta \neq 0^\circ$ the pinhole is not centred with respect to the optical axis. Note that the pinhole diameter D_{Ph} effectively limits the numerical aperture of the microscope

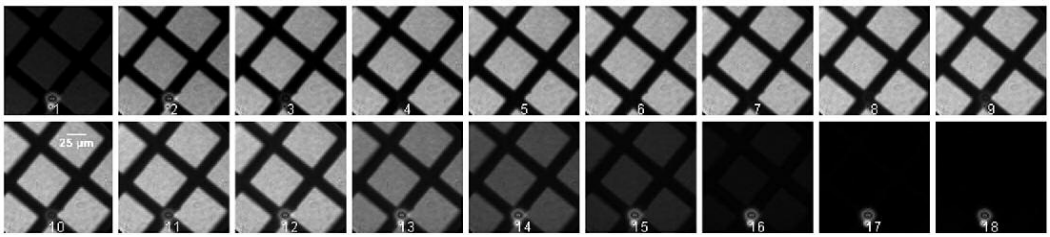

(a) Raw data acquired with a 200 μm stray light filtering pinhole.

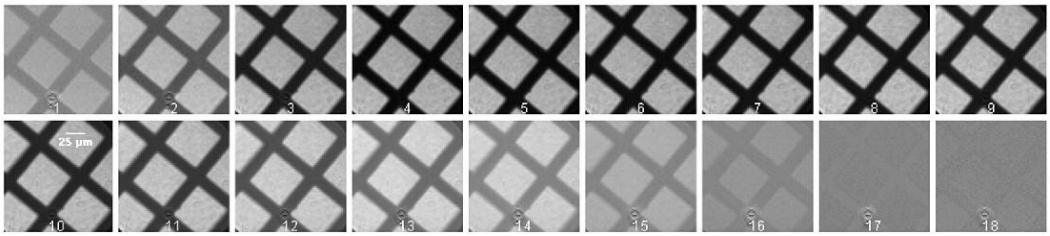

(b) Internal reflections subtracted from raw data (200 μm pinhole).

Figure 3. (a) Raw images taken at 18 different analyser azimuths A and obtained with a 200 μm stray light filtering pinhole. The internal reflections were restricted to a relatively small region at the bottom of the images. The majority of the field of view was absolutely free of spurious stray light (cf figure 4). (b) Unfortunately subtraction of internal-reflection images could not remove all artefacts. All images were recorded at an incident angle $\Theta = 46.6^\circ$ and $P = 45^\circ$. The MgF_2 layer deposited on the cover slide had two different heights: 162 nm (grating) and 249 nm (plateaux).

and thus reduces its lateral resolution. This influence was investigated experimentally and the results are given in section 6.

In figure 3 raw images of a measurement with a pinhole size of 200 μm are shown. For this small pinhole size, spurious reflexes were only visible at the very bottom of the field of view. Because of the influence of the pinhole on the lateral resolution larger pinhole sizes would be favourable. Unfortunately, the region affected by stray light increased with the pinhole diameter. Subtraction of images of the internal reflection did not remove this artefact completely (figure 3(b)). These background images were recorded by mounting a 1 cm thick glass plate (BK7, $n = 1.5187$, Schott, Mainz, Germany) with immersion oil to the objective. As the refractive indices were matched this ensured that there was no light reflected at this interface and only the internal reflections created by the illuminating beam were recorded by the CCD camera. For the 200 μm pinhole the region affected by spurious stray light was relatively small. Outside this region, the reduction of internal stray light was remarkable: dividing for each analyser azimuth A the images of the internal reflections by measurements at a sample yielded the background-to-signal ratio (cf figure 4). Frequently, the intensity of the recorded background-images was zero and in order to improve the readability of the logarithmic plot they were laterally averaged (Gaussian with a radius of 12 pixels). It could be estimated that the residual intensities were due to the shot and read-out noise of the CCD camera. Comparing the measured background-to-signal ratio to the results found in [25], it was obvious that subtraction of internal-reflection images was no longer necessary.

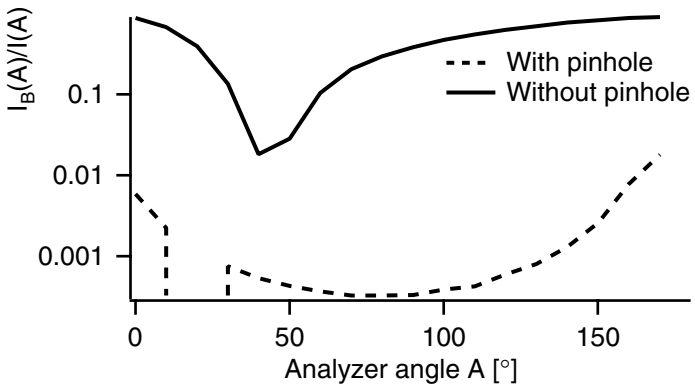

Figure 4. Shown are intensities $I_B(A)$ of the measured background images divided by intensities $I(A)$ obtained from measurements at a sample (73.8 nm MgF_2, $\Theta = 46.6°$, $P = 45°$). Comparing data with (broken line) and without the stray light trap (thick line) shows that spurious stray light is greatly reduced. Note the logarithmic scale.

5.2. Ellipsometric performance

The addition of the pinhole suppressed the stray light very effectively. Because of this, we could compare the measured and theoretically expected ellipsometric quantities by the methods we had developed for silicon substrates [21]: for measurement, we chose an incident angle $\Theta = 46.6°$ close to the pseudo Brewster angle of the system [25]. The samples were measured at polarizer settings $P = \pm 45°$. The measured intensities were subsequently corrected for the slight nonlinearity of the CCD camera and averaged of homogeneous regions (ca 35 μm $\times$ 35 μm). Later we will show that averaging could also be omitted. The ellipsometric angles Ψ and Δ were calculated from these corrected and averaged values. The resulting ellipsometric quantities were zone averaged [29, 30], i.e. the Ψ and Δ pairs measured at polarizer settings $P = 45°$ and $P = -45°$ were averaged. This procedure eliminates certain systematic errors (mainly component azimuthal angle errors δA, δP and δC) to first order. These experimental data—obtained from measurements with and without compensator—were compared to the theoretically expected values for the particular composition of planar stratified layers of each sample (cf figure 5(a)). Compared to measurements without stray light trap (cf figure 2) the measured data were extremely smooth, but differed systematically from the theoretical data. These deviations could be attributed to instrumental polarization [31] of the imaging optics.

The influence of the imaging optics on the polarization can be accounted for by applying the model presented and verified experimentally in [25]. In this model the imaging optics is treated formally exactly as the sample itself: it contributes its own ellipsometric quantities Ψ_{Obj} and Δ_{Obj} to the measurement. The ellipsometric measurements Ψ' and Δ' of the combined system 'imaging system + object' can be corrected for the influence of the imaging system with the help of the following correction laws:

$$\tan \Psi' = \tan \Psi \tan^2 \Psi_{Obj}, \tag{23}$$

$$\Delta' = \Delta + 2\Delta_{Obj}. \tag{24}$$

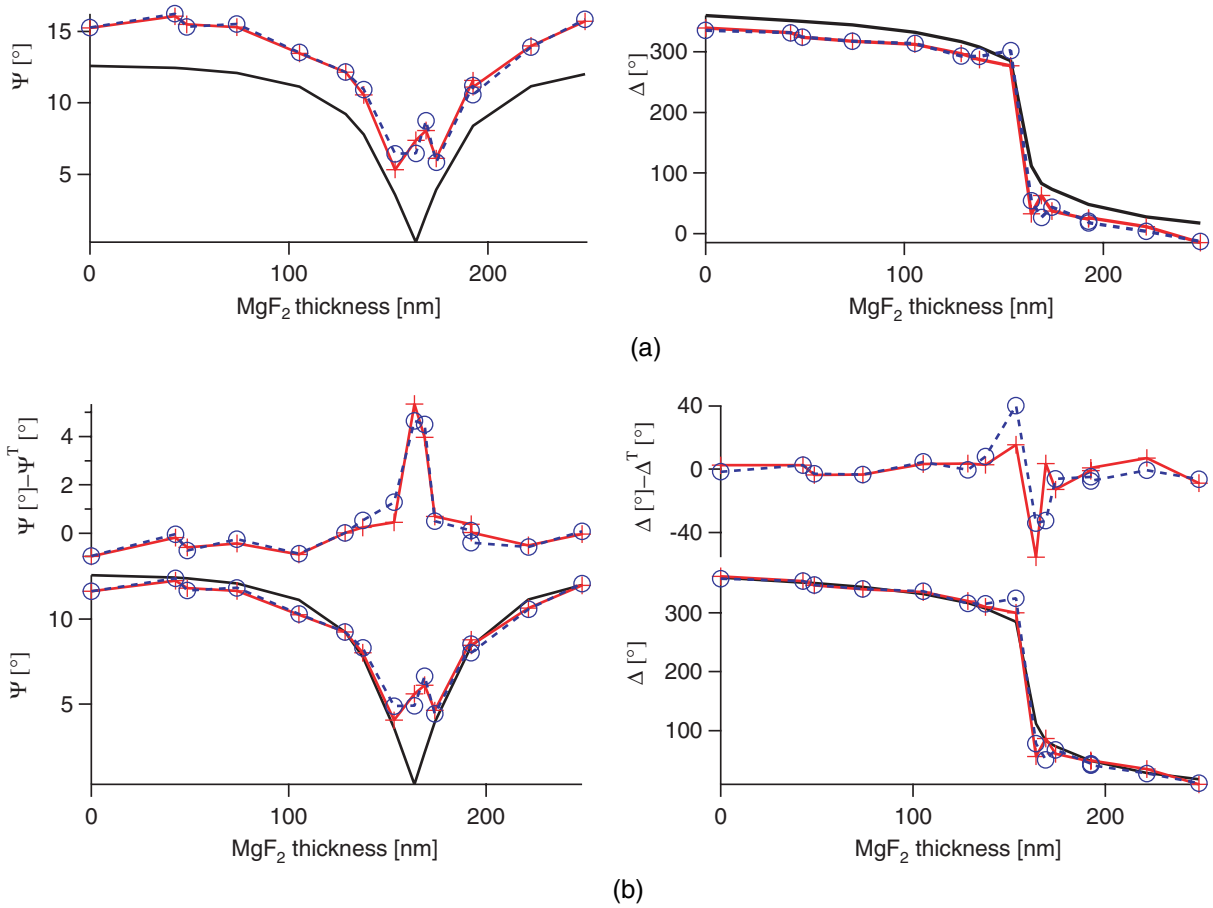

Figure 5. (a) Measurements at the glass–water interface with the stray light trap: measured data ($\Theta = 46.6^\circ$, $P = 45^\circ$)—already linearized and zone averaged—in comparison to theoretical data (thick line, black). Measurements with (crosses, red) and without (circles, blue) compensator were in excellent agreement, but exhibit systematic deviations to theoretical expected data. (b) Correcting for instrumental polarization brought the measured data in excellent agreement with the expected data (see the residuals shown).

Using the data shown in figure 5 it is possible to obtain the parameters Ψ_{Obj} and Δ_{Obj} of the utilized imaging optics by minimizing the sum

$$\sum_i \left(\Psi_i^T - \tan^{-1}\left(\frac{\tan \Psi_i'}{\tan^2 \Psi_{\text{Obj}}} \right) \right)^2 + (\Delta_i^T - (\Delta_i' - 2\Delta_{\text{Obj}}))^2, \tag{25}$$

where Ψ_i^T and Δ_i^T are the theoretically expected values and Ψ_i' and Δ_i' are the experimentally determined (nonlinearity corrected and zone averaged) ellipsometric quantities of figure 5. This yielded $\Psi_{\text{Obj}} = 49.0^\circ$ and $\Delta_{\text{Obj}} = -11.6^\circ$ for the correction parameters.[3] After correction for

[3] Here data exhibiting large residuals (data points #9 and #10) were excluded from the minimization. This is justified as values of $\Psi < 5^\circ$ that cannot be measured accurately and Δ-values near the discontinuity depend strongly on small experimental errors (Θ, refractive index of water and small errors in the assumed layer thickness). For completeness the resulting values for inclusion of *all* data points are given: $\Psi_{\text{Obj}} = 49.3^\circ$ and $\Delta_{\text{Obj}} = -13.1^\circ$.

instrumental polarization the data were in very good agreement with the theoretically expected values (figure 5(b)). Only in the region where Ψ exhibits a minimum and Δ is discontinuous, the residuals became very large. This can be explained by looking at the laws of error propagation (26) and (27), derived from (8) and (9):

$$\delta\Psi = \frac{1}{4}\frac{\cos^2\Psi}{\tan\Psi}\left(\frac{\tan^2 P + \tan^2\Psi}{\tan P}\right)^2 \delta a \overset{P\equiv\Psi}{=} \tfrac{1}{2}\sin(2\Psi)\delta a, \tag{26}$$

$$\delta\Delta = \sqrt{\frac{(\tan^2 P + \tan^2\Psi)^2\,\delta b^2 + (1/4)((\tan^3 P/\tan\Psi) - (\tan^3\Psi/(\tan P))\cos^2\Delta\,\delta a^2}{4\,\tan^2 P\,\tan^2\Psi\,\sin^2\Delta}}$$
$$\overset{P\equiv\Psi}{=} -\frac{\operatorname{sgn}(\Psi)}{|\sin\Delta|}\,\delta b. \tag{27}$$

Near $\Psi \approx 0^\circ$ errors in $\delta\Psi$ and $\delta\Delta$ tend to diverge. In this region, the ellipsometric quantities become extremely sensitive to small experimental errors. This kind of singularity is inherent to measurements with and without compensator. Unfortunately, this behaviour cannot be avoided, because the usual strategy to suppress propagation of errors by measuring at $P = \Psi$ [32] does not bring remedy for the system under consideration here: at such small P ($\approx \Psi$) values, second-order systematic errors become important and zone averaging becomes ineffective [30]. In addition, the already weakly reflecting sample would be measured under conditions where even less light is reflected at the sample.

5.3. Accuracy

Considering the difficulties the glass–water interface poses for ellipsometric microscopy, it is almost surprising how accurate Ψ and Δ could be determined with the presented setup. In terms of mean absolute deviations, Ψ and Δ were determined accurately up to 0.41° and 4.3°, respectively.[4] In this respect, the modified setup was almost equally accurate in determination of Ψ/Δ at the glass–water interface as on silicon substrates. However, problematic is the fact that the system under consideration does not exhibit much contrast in terms of the deposited thickness of MgF_2: Ψ varies in the range of $[0.1^\circ, 12.6^\circ]$, but the region $[0^\circ, 5^\circ]$ poses serious experimental problems. The same holds for Δ which is very prone to systematic errors in the range of [140, 175] nm. In the complementary thickness range, Δ varies by about 127°. Using a material with higher refractive index would result in a much higher ellipsometric contrast. MgF_2 was chosen because of its refractive index similarity with hydrated proteins or lipids ($n \approx 1.40$–1.48). These considerations led to the choice of one of the most demanding systems for ellipsometry.

Figure 6(a) shows the results obtained by fitting n and d simultaneously to the corrected ellipsometric data. At very small heights the obtained refractive indices and thicknesses can be meaningless. Otherwise, the agreement was surprisingly good. Note that the largest measured thickness was still far away from the period

$$D_\Theta = \frac{\lambda}{2n_j}\left(1 - \frac{n_1^2}{n_j^2}\sin^2\Theta\right)^{-\frac{1}{2}} = 324\,\text{nm}$$

[4] Because of the large influence of systematic errors in the region $\Psi \approx 0^\circ$ the data points #8, #9 and #10 of figure 5 were omitted in this estimate. Thus, the mean absolute deviation was computed from 22 values for Ψ and Δ, each.

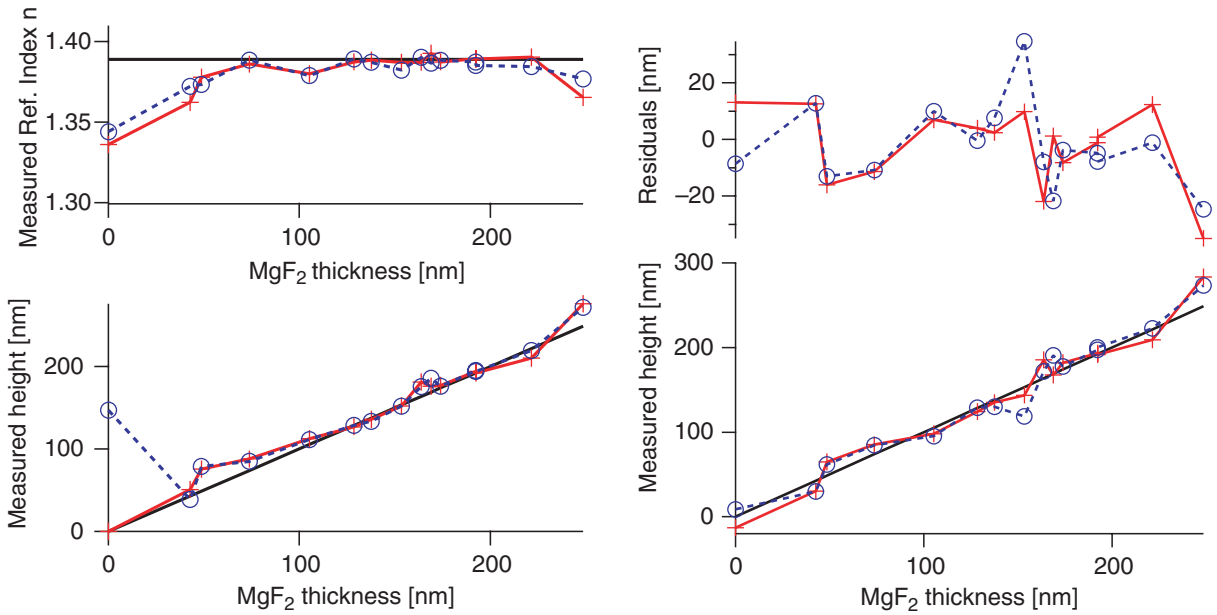

Figure 6. (a) Refractive indices and thicknesses simultaneously obtained by means of a 2D-fit from zone averaged ellipsometric data corrected for detector nonlinearities and instrumental polarization (i.e. Ψ and Δ values shown in figure 5(b)): shown are data measured with (crosses, red) and without (circles, blue) compensator. The thick line represents expected data. (b) Resulting thicknesses, if the refractive index of MgF_2 ($n = 1.389$) is imposed.

Table 1. Accuracy of the ellipsometric microscope at the glass–water interface. The average absolute deviation of the obtained thickness is about 10 nm. Because of its great susceptibility to errors the first data point of the graphs presented in figure 6 was excluded for computation of the mean absolute deviation.

		2D fit		1D fit
Material	Parameters	$\overline{\lvert\Delta d\rvert}$ (nm)	$\overline{\lvert\Delta n\rvert}$	$\overline{\lvert\Delta d\rvert}$ (nm)
MgF_2	$\Theta = 46.6^\circ$, $P = 45^\circ$	8.8	5.8×10^{-3}	10.9

of the ellipsometric quantities ($n_1 = 1.5187, n_j = 1.389$). Thus, a similar reduction of the accuracy as observed for very thin films was not observed at the far end of the observed thickness range. Figure 6(b) presents the results obtained when the refractive index is imposed, i.e. the thicknesses were obtained by means of a 1D fit. The mean average deviation of the found quantities with respect to the expected values is summarized in table 1. Refractive indices were found to be about 0.6% accurate. Thicknesses can be obtained with an average accuracy of 10 nm. Both fits, 2D and 1D, were surprisingly stable with respect to the utilized starting value: only the first data point shown in figure 6 varied when starting values far from the expected thicknesses were utilized.

In order to show that retrieval of thicknesses was not only possible for ellipsometric quantities obtained from laterally averaged intensities, figure 7 presents full-frame Ψ- and

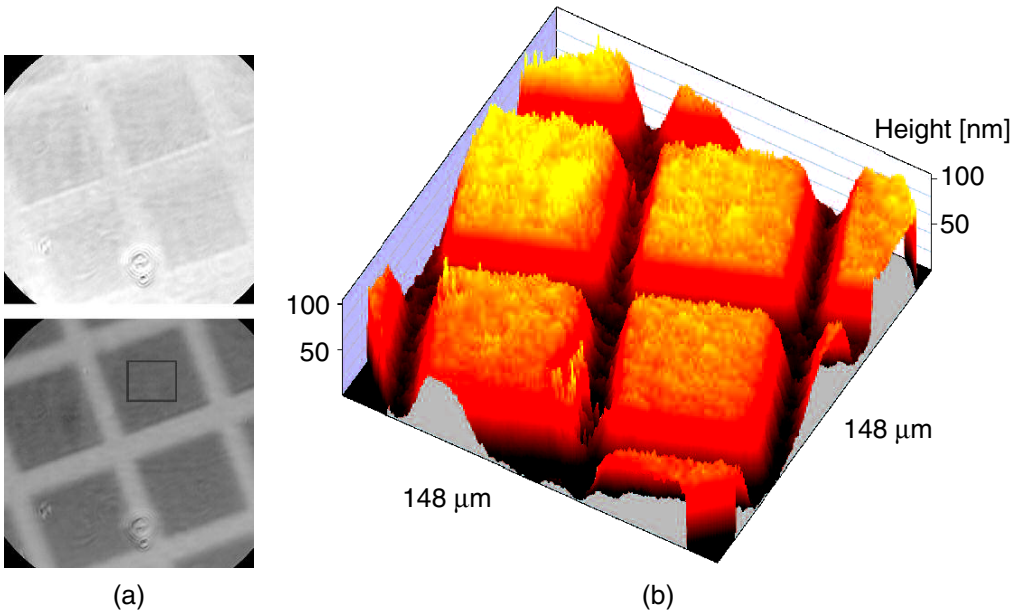

Figure 7. (a) Contrast enhanced images of Ψ (top) and Δ (bottom) (sample: 74 ± 5 nm MgF_2 at the glass–water interface, $\Theta = 46.6°$, $P = 45°$). The rectangle marks the region from which the histograms shown in figure 8 were obtained. (b) 3D plot of the thicknesses obtained by means of a 1D fit. The residual stray light reflex causes distortion of the obtained thicknesses. Fortunately this effect is restricted to a very small region.

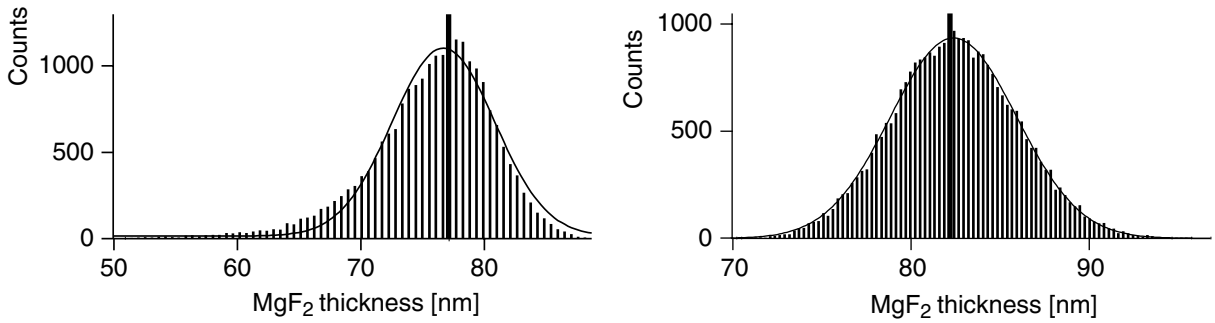

Figure 8. Histogram of the thicknesses within the rectangular region marked in figure 7(a). A Gaussian fit to the histogram of data obtained from measurements with (right) and without (left) compensator yielded mean heights of 82.3 ± 5 nm and 76.7 ± 6 nm, respectively. The vertical thick bars mark the thickness obtained by laterally averaging the intensities within the same region.

Δ-maps. In addition, a 3D-plot of the thicknesses obtained at each single pixel is shown. At the present stage, the recorded pictures suffer from vignetting because of the too small radii of lenses 6 and 7. In addition, the effect of residual stray light is clearly visible. Fortunately, this artefact is restricted to a relatively small region at the very bottom of the images. Figure 8 shows histograms of thicknesses obtained at single pixels (with and without compensator) in comparison

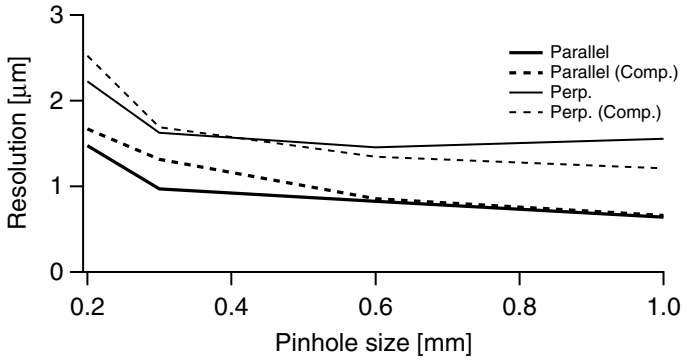

Figure 9. Influence of the stray light filtering pinhole on the lateral resolution (measured at the silicon–air interface, $\Theta = 53.1^\circ$, $P = 45^\circ$): shown are maximum, i.e. worst case values obtained from intensity profiles across three different step heights (25, 103 and 137 nm) as a function of the diameter of the stray light filtering aperture. A significant deterioration was not observed for pinhole diameters larger than 300 μm.

to thicknesses obtained from laterally averaged intensities (thick vertical bar). A Gaussian fit to the histograms yielded mean heights of 82.3 ± 5 nm and 76.7 ± 6 nm for thicknesses obtained from data measured with and without compensator, respectively. The amplitude of the noise limits the height sensitivity and thus we find a vertical sensitivity of approximately 5 nm.

6. The influence of the stray light pinhole on the lateral resolution

The stray light pinhole eliminated the spurious internal reflections very effectively. However, this pinhole also limited the numerical aperture and hence degraded the lateral resolution of the microscope. In order to estimate its influence on the lateral resolution a series of experiments with varying pinhole diameters were made. Because glass substrates with sharp structures were not available, these experiments were performed at the air–silicon interface, using the silicon substrates with etched structures already described in [21]. Note that these samples had to be measured with a dry objective (MPlanApo 50×, NA = 0.95, Olympus). These are the only measurements presented here that were performed at the silicon–air interface, all others took place at the glass–water interface. We used the ISO standardized *knife-edge method* [33] for retrieval of an objective and reproducible estimate of the lateral resolution. The samples were illuminated under a certain angle of incidence and therefore different lateral resolutions are expected for various orientations of the structures. Because of coherent superposition of neighbouring Airy patterns the observed resolution is dependent on their phase relation. This is why the measured resolution might be dependent on the layer composition of the sample (material and thicknesses). Therefore we measured samples with different heights and took the maximum value as a measure for the lateral resolution (for more details see [21]). The results are shown in figure 9. A significant deterioration of the lateral resolution was only observed for the 200 μm pinhole. We did not attempt to find a quantitative model for the observed behaviour. The utilized part of the objective exit pupil aperture that is located at its very edge, where lens performance is lowest (cf figure 10): these regions are expected to exhibit a reduced transmission ability due to the large angles of

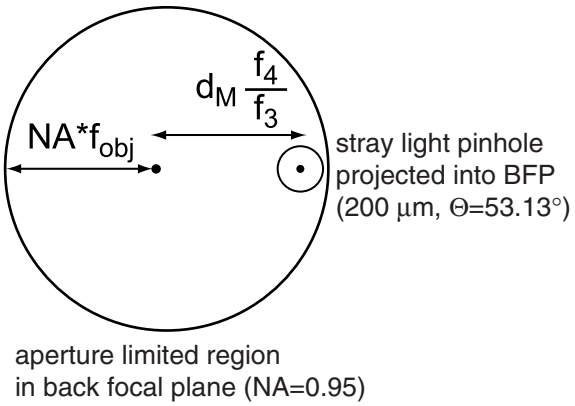

Figure 10. Projection of the 200 μm stray light filtering pinhole into the back focal plane (true to scale).

incidence of the collected light rays. This would have to be incorporated in any accurate model. However, the pinhole size for which the sudden increase of the lateral resolution limit of structures perpendicular to the plane of incidence was observed coincided with the prediction of a very simple model. The slope of the curve should suddenly increase when the pinhole diameter starts to constrain the diffraction orders from both sides, i.e. if the radius of the projected pinhole $(D_{\mathrm{Ph}}/2) \cdot (f_5/f_6)(f_4/f_3)$ touches the border of the backfocal aperture:

$$d_{\mathrm{M}} \frac{f_4}{f_3} + \frac{D_{\mathrm{Ph}}}{2} \frac{f_5}{f_6} \frac{f_4}{f_3} = \mathrm{NA}\, f_{\mathrm{Obj}}. \tag{28}$$

For the utilized objective (MPlanApo 50×, NA = 0.95, Olympus, $f_{\mathrm{Obj}} = 3.6$ mm) and an angle of incidence $\Theta = 53.13^\circ$ ($d_{\mathrm{M}} = 1.8$ mm) a pinhole diameter of 225 μm in accordance with the measurements was found. Transferring this to measurements at the glass–water interface, the limit of the pinhole diameter is estimated at 320 μm (NA = 1.4, $f_{\mathrm{Obj}} = 2.61$ mm, $d_{\mathrm{M}} = 1.8$ mm). Of course, this would have to be validated by experiments at the glass–water interface.

7. Conclusion

We presented a setup which enabled us to perform spatially resolved ellipsometric measurements of thin films at the glass–water interface. Because this system suffers from low ellipsometric contrast the accuracy of the obtained heights was considerably reduced to 10 nm, although the accuracy of the ellipsometric angles was close to that achieved at silicon interfaces. Nevertheless, refractive indices can be obtained with an astonishing accuracy of 0.6%. In view of the intrinsic difficulties of the glass–water interface for ellipsometry, a very good ellipsometric performance at high lateral resolution was achieved.

Acknowledgments

We are grateful to Professors E Sackmann and M Rief for hospitality and continuous support. The microstructured silicon samples were a gift of Ms C M Cesa.

References

[1] Singhvi R *et al* 1994 *Science* **264** 696
[2] Chang J C, Brewer G J and Wheeler B C 2003 *Biomaterials* **24** 2863
[3] Vogt A K *et al* 2004 *J. Neurosci. Methods* **134** 191
[4] Jenkins A T A, Neumann T and Offenhausser A 2001 *Langmuir* **17** 265
[5] Hovis J S and Boxer S G 2001 *Langmuir* **17** 3400
[6] Goennenwein S, Tanaka M, Hu B, Moroder L and Sackmann E 2003 *Biophys. J.* **85** 646
[7] Palacek S P, Schmidt C E, Lauffenburger D A and Horwitz A F 1996 *J. Cell Sci.* **109** 941
[8] Kirfel G, Rigort A, Borm B, Schulte C and Herzog V 2003 *Cell Motil. Cytoskeleton* **55** 1
[9] Curtis A S G 1964 *J. Cell Biol.* **20** 199
[10] Pluta M 1989 *Advanced Light Microscopy* vol 2 *Specialized Methods* (New York: Elsevier)
[11] Wiegand G, Neumaier K R and Sackmann E 1998 *Appl. Opt.* **37** 6892
[12] Schilling J, Sengupta K, Goennenwein S, Bausch A R and Sackmann E 2004 *Phys. Rev.* E **69** 021901
[13] Zhan Q and Leger J R 2002 *Appl. Opt.* **41** 4630
[14] Erman M and Theeten J B 1986 *J. Appl. Phys.* **69** 859
[15] Cohn R F, Wagner J W and Kruger J 1988 *Appl. Opt.* **27** 4664
[16] Albersdörfer A, Elender G, Mathe G, Neumaier K R, Paduschek P and Sackmann E 1998 *Appl. Phys. Lett.* **72** 2930
[17] Liu A-H, Wayner P C and Plawsky J L 1994 *Appl. Opt.* **33** 1223
[18] Beaglehole T 1988 *Rev. Sci. Instrum.* **59** 2557
[19] Jin G, Jansson R and Arwin H 1996 *Rev. Sci. Instrum.* **67** 2930
[20] Harke H, Teppner R, Schulz O, Orendi H and Motschmann H 1997 *Rev. Sci. Instrum.* **68** 3130
[21] Linke F and Merkel R 2005 *Rev. Sci. Instrum.* at press
[22] Azzam R M A and Bashara N M 1996 *Ellipsometry and Polarized Light* (Amsterdam: North-Holland)
[23] Hauge P S and Dill F H 1973 *IBM J. Res. Develop.* **17** 472
[24] Neumaier K R, Elender G, Sackmann E and Merkel R 2000 *Europhys. Lett.* **49** 14
[25] Linke F and Merkel R 2004 *IEE Proc. Nanobiotechnol.* **151** 95
[26] Aspnes D E 1974 *J. Opt. Soc. Am.* **64** 812
[27] de Nijs J M M, Holtslag A and Silfhout A v 1988 *J. Opt. Soc. Am.* A **5** 1466
[28] Beuthan J, Minet O, Helfmann J, Herrig M and Müller G 1996 *Phys. Med. Biol.* **41** 369
[29] Collins R W 1990 *Rev. Sci. Instrum.* **61** 2029
[30] de Nijs J M M and Silfhout A v 1988 *J. Opt. Soc. Am.* A **5** 773
[31] Chipman R A 1989 *Opt. Eng.* **28** 90
[32] Aspnes D E 1974 *J. Opt. Soc. Am.* **64** 639
[33] International Organization for Standardization (Geneva) 2000 *Photography—Electronic Still-Picture Cameras—Resolution Measurements* ISO 12233